The Astrophysical Journal, 971:61 (10pp), 2024 August 10 https://doi.org/10.3847/1538-4357/ad5a0b
© 2024. The Author(s). Published by the American Astronomical Society.
OPEN ACCESS

Photometry of Saturated Stars with Neural Networks

Dominik Winecki[1] and Christopher S. Kochanek[2,3]
[1] Department of Computer Science and Engineering, The Ohio State University, Columbus, OH 43210, USA
[2] Department of Astronomy, The Ohio State University, 140 W. 18th Ave., Columbus, OH 43210, USA; kochanek.1@osu.edu
[3] Center for Cosmology and AstroParticle Physics, The Ohio State University, 191 West Woodruff Ave., Columbus, OH 43210, USA
Received 2024 April 23; revised 2024 June 10; accepted 2024 June 18; published 2024 August 6

Abstract

We use a multilevel perceptron (MLP) neural network to obtain photometry of saturated stars in the All-Sky Automated Survey for Supernovae (ASAS-SN). The MLP can obtain fairly unbiased photometry for stars from $g \simeq 4$ to 14 mag, particularly compared to the dispersion (15%–85% 1σ range around the median) of 0.12 mag for saturated ($g < 11.5$ mag) stars. More importantly, the light curve of a nonvariable saturated star has a median dispersion of only 0.037 mag. The MLP light curves are, in many cases, spectacularly better than those provided by the standard ASAS-SN pipelines. While the network was trained on g-band data from only one of ASAS-SN's 20 cameras, initial experiments suggest that it can be used for any camera and the older ASAS-SN V-band data as well. The dominant problems seem to be associated with correctable issues in the ASAS-SN data reduction pipeline for saturated stars more than the MLP itself. The method is publicly available as a light-curve option on ASAS-SN Sky Patrol v1.0.

Unified Astronomy Thesaurus concepts: CCD photometry (208); Time domain astronomy (2109); Algol variable stars (24); Computational methods (1965)

1. Introduction

Projects such as the All-Sky Automated Survey for Supernovae (ASAS-SN; Shappee et al. 2014; Kochanek et al. 2017; Hart et al. 2023), the Asteroid Terrestrial-impact Last Alert System (ATLAS; Tonry et al. 2018b), and the Zwicky Transient Facility (ZTF; Bellm et al. 2019) currently monitor all (ASAS-SN and ATLAS) or large fractions (ZTF) of the visible sky and provide public access to their data. For ASAS-SN, this consists of its catalog of variable stars (Jayasinghe et al. 2019), ASAS-SN Sky Patrol (Kochanek et al. 2017), which will provide an uncensored light curve for any user-requested sky coordinate, and ASAS-SN Sky Patrol v2.0 (SP2; Hart et al. 2023), which provides continuously updated light curves of roughly 100 million sources from asteroids to stars and quasars. In the near future, the Vera Rubin Observatory (e.g., Ivezić et al. 2019) will provide ZTF-like coverage and cadence for far fainter sources.

Professional astronomy has lost, however, the ability to monitor the bright sky—the need for both funding and efficient operations drive projects toward fainter and more numerous sources. Yet these very bright sources are the ones which will have the best stellar spectroscopic observations from projects like the Sloan Digital Sky Survey (SDSS)/APOGEE (e.g., Abdurro'uf et al. 2022) or Gaia (e.g., Gaia Collaboration et al. 2023) including either indications of binarity or full orbital solutions.

The problem is that charge coupled device detectors have a finite dynamic range above which a pixel is saturated. A typical dark time ASAS-SN image has a sky background of ∼200 counts and saturates at ∼60,000 counts. The point-spread function (PSF) has an FWHM of roughly 2 pixels (Shappee et al. 2014; Kochanek et al. 2017), leading to a point-source dynamic range of roughly 7 mag from $g \sim 11.5$ to $g \sim 18.5$ mag. This leaves some $\sim 10^6$ stars that are saturated in ASAS-SN observations. The excess charge of the saturated pixels then bleeds into pixels along the read direction of the detector.

ASAS-SN inherited from the original All-Sky Automated Survey (ASAS; Pojmanski 2002) one method of trying to obtain photometry of saturated stars. The pipeline tries to identify the flux in the bleed trails of the saturated stars and then adds a Gaussian with that flux at the star's location. The bleed trails are then replaced by linear interpolation of the adjacent, unsaturated pixels. This approach has also been applied to Swift/UVOT data by Page et al. (2013). As shown by some of the examples in Kochanek et al. (2017), this procedure frequently works surprisingly well. An alternative approach is to model the unsaturated wings of the PSF (e.g., Su et al. 2022; Zhou et al. 2023).

Here, we experiment with a new approach, namely, training a multilevel perceptron (MLP) neural network to do photometry of saturated stars. Convolutional neural networks (CNNs) have been used successfully for a range of astronomical problems, such as star–galaxy classification (Kim & Brunner 2017), transient classification (Qu et al. 2022), and photometric redshifts (Pasquet et al. 2019). There have been some applications of CNNs to photometry (Yang et al. 2023; Yuan et al. 2023) but not to the specific problem of saturated star photometry. Our data consists of small, nonrectangular images centered on each target star, and the relevance of each input pixel is highly dependent on its position, so an MLP seemed a better choice for this purpose than a CNN. The theory is that a network can simply learn the sensor-specific behavior for stars of different levels of saturation and then predict the true brightness. In Section 2 we describe the construction of the training set, and in Section 3 we describe the model and the training process. We present the results in Section 4 with comparisons to the results produced with aperture photometry on subtracted images by ASAS-SN SP2 (Hart et al. 2023). We

Original content from this work may be used under the terms of the Creative Commons Attribution 4.0 licence. Any further distribution of this work must maintain attribution to the author(s) and the title of the work, journal citation and DOI.

discuss the results, known problems, potential solutions, and possible future improvements in Section 5.

2. Training Data

We selected stars from Gaia Data Release 3 (DR3; Gaia Collaboration et al. 2016, 2023) that were observed by the "bi" camera of the ASAS-SN Bohdan Paczynski mount at CTIO in Chile. We selected a random 40,000 nonvariable stars (based on Gaia DR3, Eyer et al. 2023) over the sky per 1 mag wide bin starting at $G = 2$ mag. This provides a training set roughly uniformly distributed in magnitude. Obviously, the very brightest bins have fewer than 40,000 stars and so we were simply including all available stars. We kept stars observed by bi, with defined G, B_P, and R_P magnitudes.

Each target then has hundreds of epochs of ASAS-SN observations, so we randomly selected ∼4 images per target and extracted a 21 pixel square "postage stamp" image of the target. We used single exposures interpolated to the astrometric frame of the reference image. Only images flagged as having been taken in good conditions were used and the postage stamp edges had to be at least 50 pixels from the detector edges. We generated ∼332,000 postage stamps spanning $G = 3$ to 15 mag.

We predict the g-band magnitudes from the Gaia DR3 magnitudes because the Gaia magnitudes homogeneously span the full range we consider. We first applied the Gaia EDR3 saturation corrections from Riello et al. (2021; these affect $G < 8$ for G, $G < 3.94$ for B_P, and $R_P < 3.45$ for R_P) and estimate the g-band magnitude from the corrected G, B_P, and B_P magnitudes following Riello et al. (2021). The reported scatter for these estimates is 0.075 mag. We then convert to the estimated counts in an image using the zero-point Z of the ASAS-SN reference image and the mean transparency correction t between fluxes on the reference image and the target image determined by ISIS (Alard & Lupton 1998; Alard 2000) as part of the standard ASAS-SN image subtractions (the values in `sum_kernel`). This gives predicted counts of

$$\log N_s = -0.4(g - Z) - \log t. \quad (1)$$

The ASAS-SN PSF has an FWHM of roughly 16″. At this resolution, the flux in any ASAS-SN photometric aperture can be a blend of the fluxes from multiple stars. This is not important for the brightest stars, but becomes increasingly important for fainter stars, particularly at lower Galactic latitudes. To mitigate this, we found all $G < 20$ mag Gaia DR3 stars within 1′ of each target star. We computed a G-band flux correction f_c factor to go from the flux of the target star to the total flux of all stars within 8″. Assuming that the network will "learn" about background subtraction, we need to correct this contaminating flux for the median stellar background flux contribution, b_c, to the signal region. Hence, we rescale the prediction for the number of counts as

$$N_s \rightarrow N_s(1 + f_c) - b_c. \quad (2)$$

When we added bias subtraction to the ASAS-SN pipelines, we started to damage the cores of the images of saturated stars, a problem that remains to be fixed. Such stars are identifiable by the presence of pixels that are exactly unity because the final consequence of the problem is that the modified ASAS pipeline declares them to be bad pixels and resets them to unity. Postage stamps with more than four such pixels are rejected for training and validation.

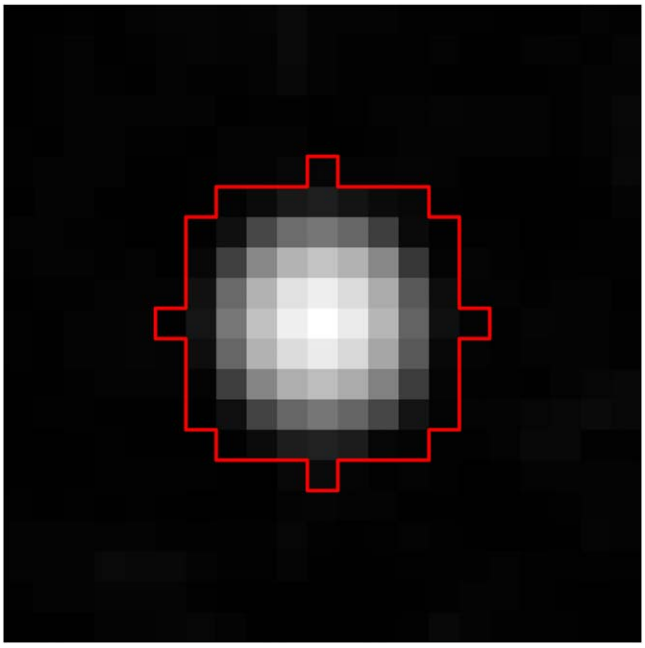

Figure 1. A log-scale image of the postage stamp of a 99.9th percentile bright star with a red contour drawn to show which pixels are used in our model.

3. Methods

In our data set, the target star never covered more than a few pixels in any direction, even at the highest brightness levels. As a preprocessing step, we reduced the analyzed region of each postage stamp to a 5 pixel radius circle around the center. This is to help focus the model training on the relevant region and to give less context for a model to memorize. A sampling of the brightest stars found that a 5 pixel radius would capture most visible detail with a ∼1–2 pixel margin, as shown in Figure 1.

As an easy way to expand the training set, we also considered reflections of the postage stamps, adding three new postage stamps flipped horizontally, vertically, or both. This grows the training set from ∼332,000 stamps to ∼1.33 million stamps. To the extent that the ASAS-SN PSF is not circularly symmetric, this is like moving the postage stamp to the corresponding reflection of its position on the detector. We expected this to be a safe way of trivially multiplying the training set. We tracked the results for both the original and permuted orientations and were unable to find significant differences in the results.

Neural networks operate on the data turned into "tensor data," which is simply a one-dimensional array. We can also append metadata to the end of the training data, where we experimented with adding the reference image zero-point Z and the estimated sky brightness of the individual image S. We discuss other possible metadata that could be used in the discussion.

The overall training set is then divided into training (60%), testing (20%), and validation sets (20%). We were concerned about the potential for the network to memorize the expected properties of a particular star based on the pattern of surrounding background stars. To make sure this was not an issue while validating the results, all images of a particular star were placed in the same subset.

4. Results

We carried out our analysis using PyTorch (Paszke et al. 2019), optimizing the mean squared error (MSE) loss function

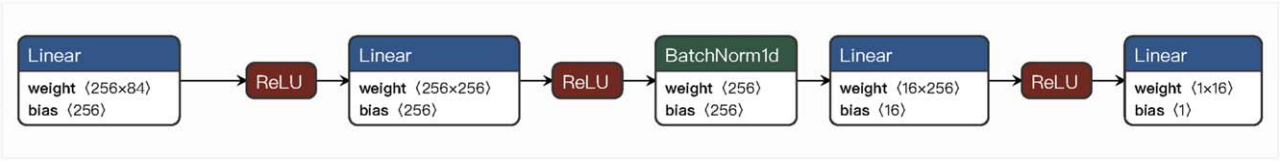

Figure 2. Final Model Architecture.

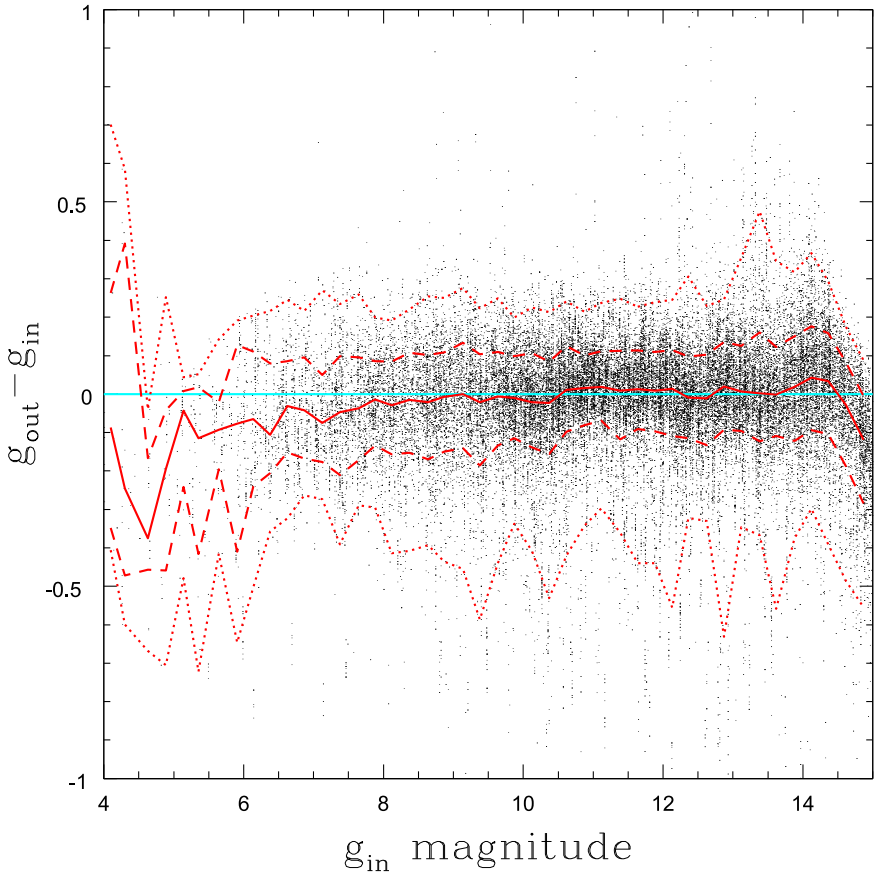

Figure 3. The differences between the input (g_{in}) and output (g_{out}) magnitudes for the verification stars. The red curves show the median (solid), 68% (dashed), and 95% (dotted) ranges of the differences in bins of 0.25 mag. A horizontal cyan line is included where the difference is zero.

between the input estimate of $\log N_s$ and the output estimate from the network. We began by experimenting with different MLP architectures. We started with two to four smaller 64-wide layers, but found that increasing the width led to faster convergence. We ultimately settled on 256-wide layers as increasing past this led to minimal improvements. The final architecture is shown in Figure 2.

After selecting the architecture, we evaluated PyTorch's Adam, AdamW, Adadelta, Adagrad, Adamax, RMSProp, and stochastic gradient descent optimizers. We trained each model to 150 epochs with each optimizer multiple times. The Adam optimizer had the lowest losses, with AdamW coming second. The other optimizers were less reliable for this task, with some never converging. We used the Adam optimizer of Kingma & Ba (2014) for our final models, with a learning rate of 0.0001 and a batch size of 128. We trained 24 models using this architecture including the hyperparameters in the training and selected the one with the best MSE for the validation data.

The performance of the fiducial MLP model for the verification data set is shown in Figure 3. The results show little bias over 10 mag (a factor of 10^4 in flux) from $g \simeq 4$ mag to $g = 14.5$ mag. The median difference is -0.004 mag, with a clear bias appearing only for the brightest and faintest stars. The magnitude differences encompassing 68% and 95% of the stars are 0.12 and 0.34 mag, respectively, and the rms dispersion is 0.168 mag.

We also considered several possible elaborations. First, we considered whether ensemble results would perform better than the best model. For example, if we defined the ensemble model as the average of the results from the four individual models with the lowest MSE values, the rms residual did not improve. Second, we tried averaging the results for the input image and its three permutations, but again found no significant improvement. As noted earlier, many saturated stars have pixels reset to unity due to some unanticipated consequences of adding overscan corrections to the pipeline. We built an independent network trained only on objects with at least one pixel set to unity to see if this would do better than simply mixing the two populations. This model had an rms residual of 0.360 mag, far worse than the general analysis. We believe the small size of

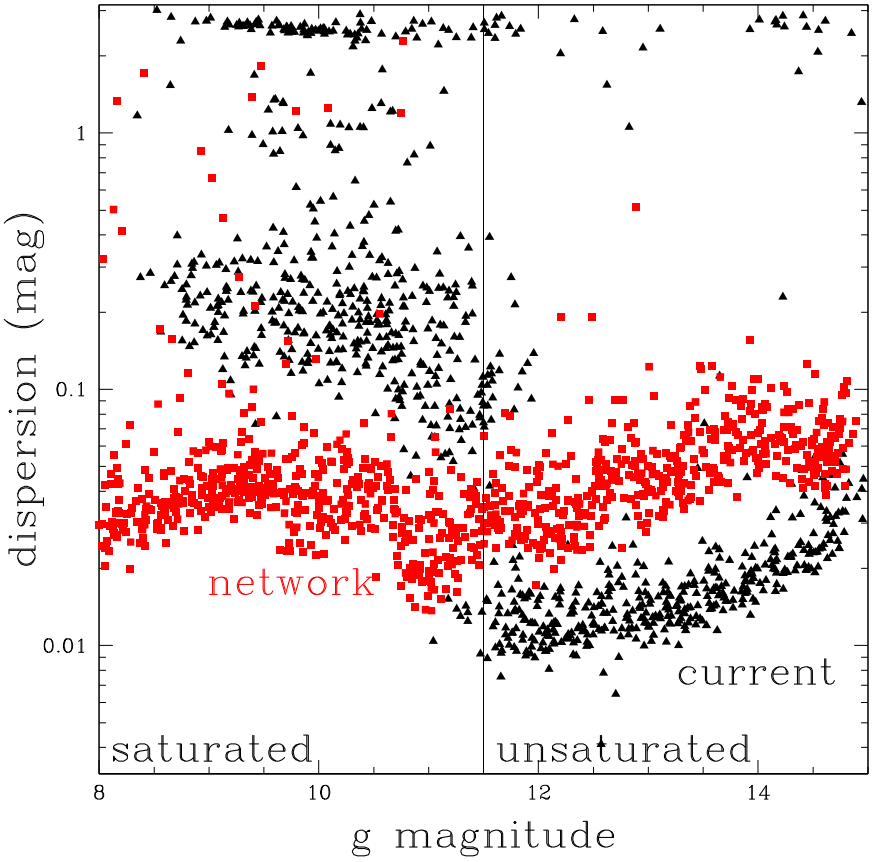

Figure 4. The light-curve dispersions of approximately 10^3 nonvariable sources as a function of g magnitude analyzed using the current SP2 pipeline (black triangles) or by the neural network (red squares). The dispersion is defined as one-half of the 15%–85% (1σ) range of the residuals about the median. The saturated (unsaturated) magnitude range is to the left (right) of the vertical line.

the resulting training set likely drives this. From this point on, we focus on our fiducial MLP model.

We looked for correlations of the residuals with distance from the detector center and Galactic latitude. We examined the distance from the center because a source of a given flux produces ∼50% fewer counts in the extreme corners of the detectors compared to the center due to vignetting. We examined the Galactic latitude because the stellar density increases rapidly for lower absolute latitudes, so the results depend more on correctly accounting for crowding by other sources under the ASAS-SN PSF. We found no significant correlation of the residuals of both the saturated and unsaturated stars with either the detector location or Galactic latitude.

Figure 3 is not really a test of our primary goal, which is to produce improved light curves rather than improved absolute photometry over the current ASAS-SN pipelines as implemented in SP2 (Hart et al. 2023). ASAS-SN epochs are generally comprised of three 90 s exposures. SP2 does aperture photometry on the coadded, subtracted images obtained for each epoch and then adds the flux of the source in the reference image. The MLP analyzes individual images since we are limited by systematic problems not photon statistics for the saturated stars. For the final MLP light curves we used the median of the results for the individual epoch images (the average if only two images, and the value if there is just one image). This procedure noticeably reduces the light-curve dispersions.

To test the performance on light curves, we randomly selected 1000 (Gaia) nonvarying sources uniformly in magnitude over $8 < g < 14.5$ mag and extracted their light curves using both the fiducial MLP model and SP2. We again limited the analysis to good images and kept only images analyzed by both pipelines. Figure 4 compares the dispersions of the MLP and SP2 light curves with at least 50 points as a function of magnitude. The dispersions are defined by one-half of the 15%–85% (1σ) range about the light-curve median. The standard pipeline has obvious problems for saturated ($g < 11.5$) images, with a large jump in the scatter from a median of 0.016 mag for $g > 11.5$ to a median of 0.22 mag for brighter sources. The band of sources with scatters above 1 mag are the ones most badly affected by the effects of the bias subtraction problem. The performance of the MLP is fairly uniform with a median scatter of 0.037 mag for the brighter sources and 0.048 mag for the fainter sources. A few of the high scatter outliers are high proper motion stars, but most are cases where the bleed trail correction algorithm has put the flux from the bleed trail in the wrong location. An obvious issue for future work is to explore why the MLP has 3 times the scatter of the standard pipeline for the unsaturated stars. Figure 5 shows eight examples of these MLP light curves. They were selected to have 15%–85% (1σ) ranges about their medians of <0.053 mag, which is true for 85% of the saturated stars (see Figure 4), but were otherwise just chosen to be the closest star to 8.0, 8.5,..., 11.5 mag.

Figures 6, 7, 8, and 9 compare the MLP light curves of Miras, Cepheids, and eclipsing binaries to those from SP2. These variables were not selected to make the MLP results look good,

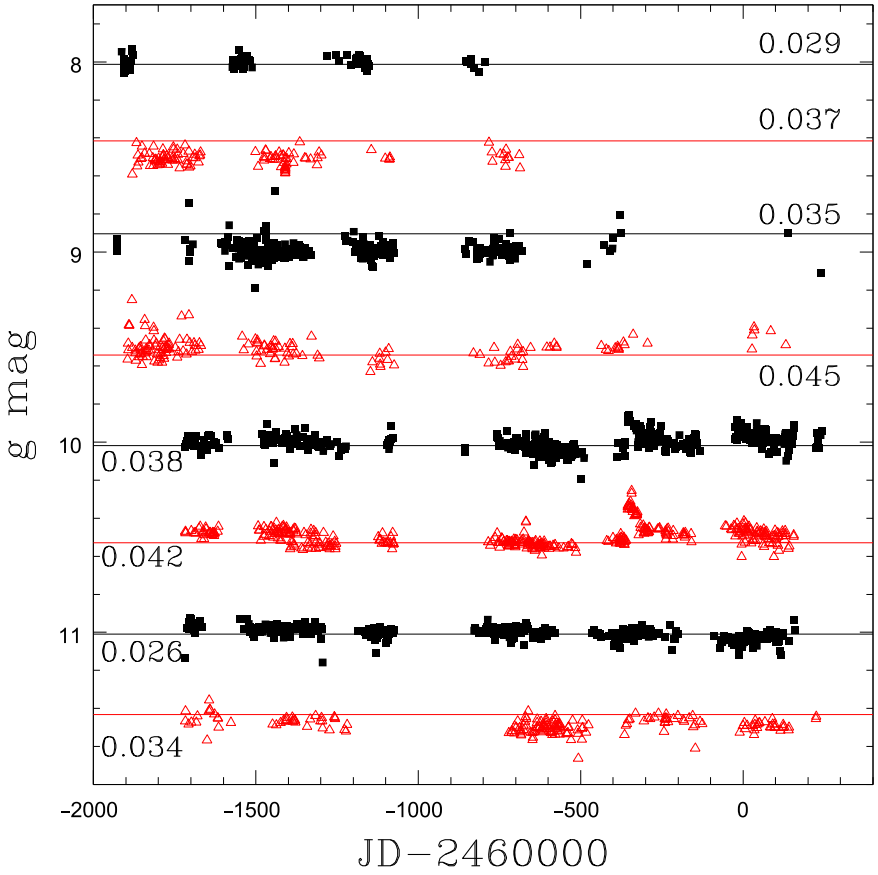

Figure 5. Light curves of the stars in Figure 4 closest to $g = 8$ mag to 11.5 mag in steps of 0.5 mag. They were also required to have 68% distribution widths less than 0.053 mag—85% of $g < 11.5$ mag stars have smaller dispersions. The horizontal lines are the Gaia-estimated g magnitudes. The number gives the dispersion estimated from the 15%–85% (1σ) range of the points about their median.

but simply to have interesting magnitudes and amplitudes for illustrating results. The Miras illustrate the ability of the MLP analysis to smoothly track the brightness of variable stars from well below the saturation limit near $g \simeq 11.25$ mag to significantly above it. While the SP2 light curves are frequently good, they start to produce significant outliers at the brightest magnitudes, particularly for X Oct. The examples of classical Cepheids include the extremely bright ℓ Car, the still naked eye visible W Sgr, and the slightly fainter R Cru. The MLP ℓ Car light curves are producing significant numbers of outliers near peak, while the SP2 light curves struggle near minimum. The W Sgr and R Cru light curves have significant numbers of faint outliers, but the MLP produces generally smoother light curves if we ignore the outliers. The MLP magnitudes are also closer to the g magnitudes predicted from the Gaia mean magnitudes. Note that since they are mean magnitudes, they should be relatively immune to any variability. The SP2 light curves are significantly fainter than the predictions and are shifted brighter by $\sim$1 mag in order to use the same magnitude ranges for both the MLP and SP2 light curves.

The driver of these problems for the bright Cepheids are two failure modes in the pipeline saturated star correction. One failure mode is to place the flux from the bleed trails at the wrong location, usually a relatively bright (but not nearly as bright) star lying nearby on the bleed trail. The second, which we do not understand, but appears to be the dominant failure for W Sgr, is to have not placed the missing flux anywhere. The saturated target appears to have been treated as part of the bleed trail and filled in by interpolation across the estimated trail.

The eclipsing binary comparisons provide the most dramatic illustration of the improvements from the MLP approach—the eclipses are clearly visible in the MLP light curves and essentially invisible in the SP2 light curves. Even CY Hyi, with its fairly high amplitude and continuous variability with phase, has a barely discernible variability pattern in the SP2 light curve. The shallow eclipses of del Cir and KV Lup are clear for the MLP light curves, as are the very narrow eclipses of TZ Men and VY Ret. The mean MLP magnitudes are close to the predicted means, while the SP2 means are again significantly fainter than predicted. There are outliers in the MLP light curves, but most could probably be eliminated with some variant of sigma clipping.

The MLP was trained using data from only a single camera (bi on the Paczynski mount), while ASAS-SN is presently comprised of 20 cameras. ASAS-SN also initially used V band, while the training data were all g-band photometry. As an experiment, we simply analyzed the data from all cameras and both filters for the stars in Figures 6, 7, 8, and 9. We "intercalibrated" the data from all the sources using a damped random walk (DRW) Gaussian process for interpolation and solving for the best light-curve means for the individual cameras and filters (these are a form of the "linear parameters" discussed in Kozłowski et al. 2010 for DRW models of quasar light curves). We found we could reduce the effects of faint outliers by dropping the faintest 10% of the light curves. Each light curve was then offset by the difference between the median light-curve mean and the mean for the individual camera and filter. This does assume that the variability

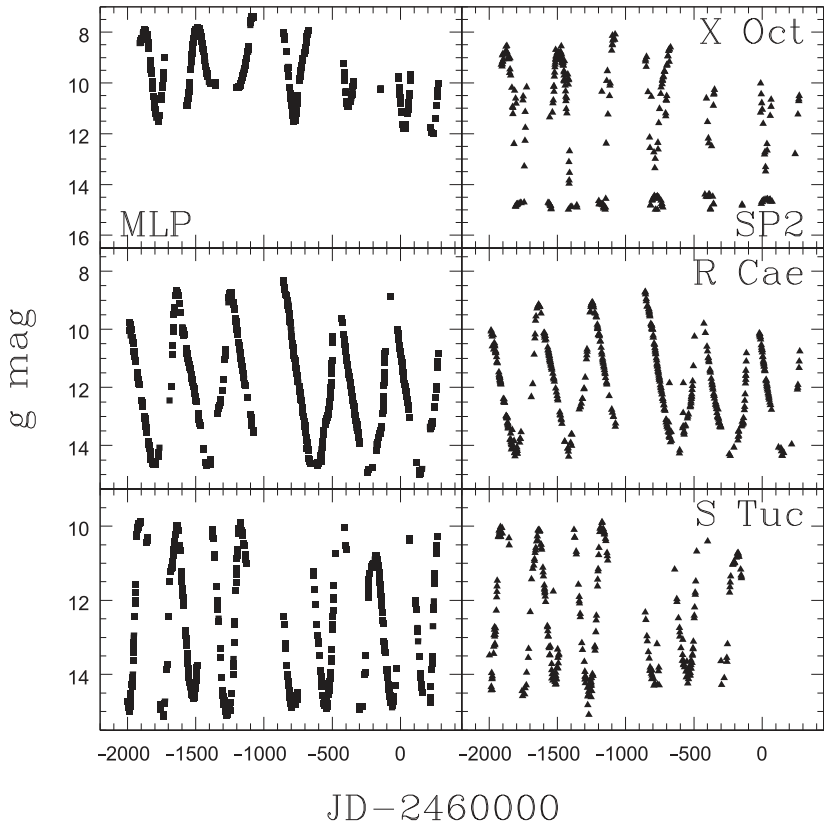

Figure 6. Light curves of Mira variables from the MLP analysis (left) and SP2 (right). While the saturated star corrections of the ASAS-SN pipeline produce surprisingly good results in many cases, the MLP pipeline results are smoother and have fewer outliers like the ones prominently seen for the SP2 light curve of X Oct. X Oct is also the example which is most saturated at peak brightness. The vertical scales are the same for both the MLP and SP2 light curves.

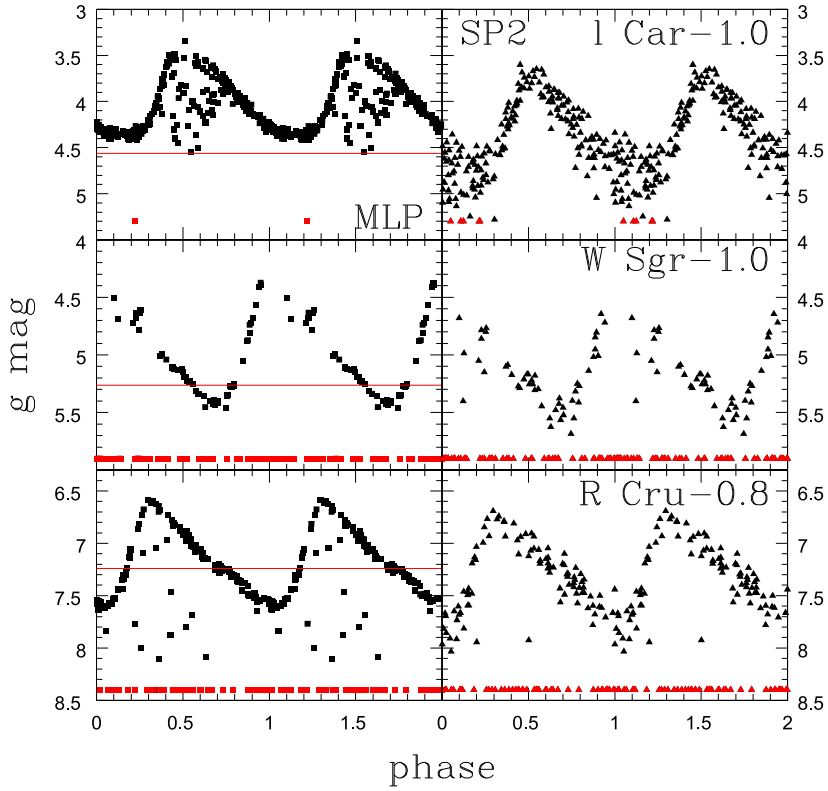

Figure 7. Light curves of very saturated Cepheid variables from the MLP analysis (left) and SP2 (right). The SP2 light curves are shifted to brighter magnitudes by the amount next to the variable name. The red points lying in a line along the bottom are outliers fainter than the minimum magnitudes of the panels. The horizontal red line is the g magnitude predicted from the mean Gaia magnitudes, which should be relatively close to the true mean magnitude. Both pipelines produce many faint outliers for W Sgr and R Cru, but the MLP light curves are arguably cleaner except for ℓ Car at peak. The vertical scales are the same for both the MLP and SP2 light curves.

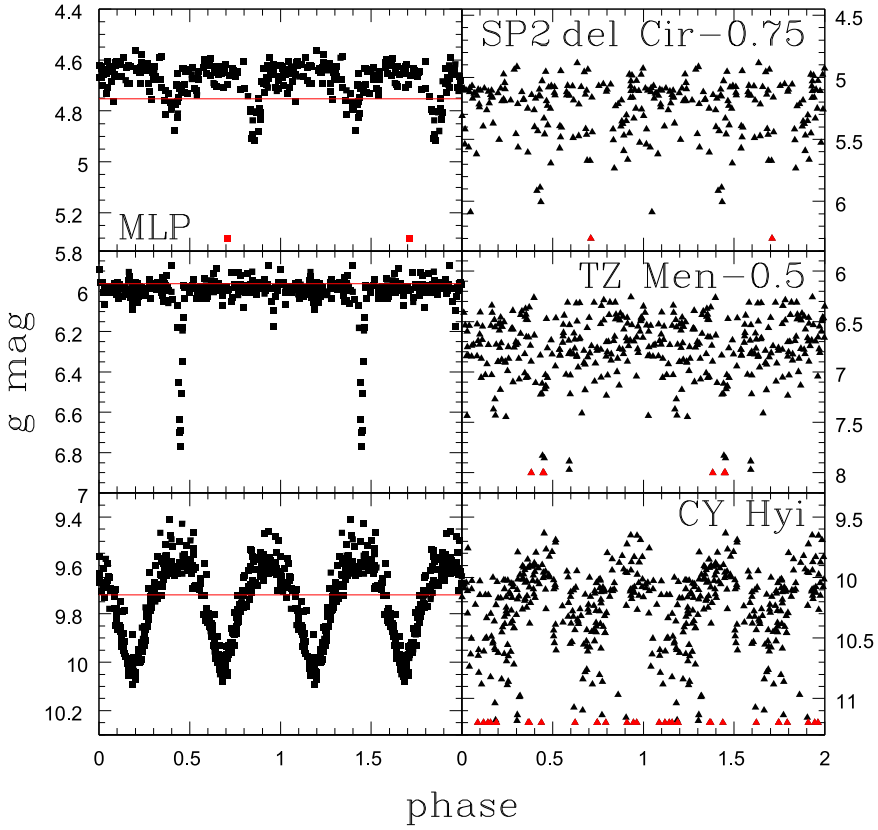

Figure 8. Light curves of eclipsing binaries from the MLP analysis (left) and SP2 (right). The SP2 light curves are shifted to brighter magnitudes by the amount next to the variable name. The bright magnitude limit is the same for the MLP and SP2 panels, but the magnitude range is generally much larger for the SP2 panels. The red points lying in a line along the bottom are outliers fainter than the minimum magnitudes of the panels. The horizontal red line is the *g* magnitude predicted from the mean Gaia magnitudes.

amplitudes and light-curve shapes are identical for the two filters, but it also the most extreme test for seeing how crucial it will be to individually train by camera and filter.

Figures 10 and 11 show the results. They are generally very good, suggesting that the current network can simply be applied generally and that we could train one MLP using data from all cameras and filters. There are outliers such as those seen for X Oct, and all the data are struggling with the bright Cepheids from Figure 10. The biggest failure is for R Cru, where the huge number of outliers has confused the intercalibration procedure. This is seen to a lesser extent for W Sgr, where too few faint outliers were rejected for the good parts of the light curves to be perfectly lined up. But for R Cae, S Tuc, and the eclipsing binaries in Figure 11, the results are extremely good.

5. Conclusions and Future Work

We developed an MLP neural network for the accurate photometry of saturated stars. The network was trained using predictions for the counts produced by the target star in a sample of ∼332,000 postage stamp images of stars roughly uniformly spread in magnitude from $g \sim 3$ to 15 mag. For the verification sample, the median magnitude differences are well within the 68% scatter of the differences (0.12 mag) except for the very brightest and faintest stars (see Figure 3). More importantly, the typical scatter in the light curve of a saturated star is only 0.037 mag (half the 15th–85th percentile range about the mean) compared to 0.22 mag for the SP2 light curves (see Figure 4). The MLP light curves of many bright variable stars are dramatically better than their SP2 light curves (see Figures 6–9) although the performance can sometimes be poor, as illustrated by the naked eye Cepheids in Figure 7 (see below). Although the network was trained using data from only one camera, it appears to work equally well when tested using data from all cameras and both *V*- and *g*-band data when combined using a Gaussian process to intercalibrate the light-curve means (see Figures 10 and 11). For some systems, this calibration procedure and/or outlier rejection would have to be done more carefully, but the results are otherwise very encouraging.

We analyzed the reduced ASAS-SN images interpolated to the frame of the reference image. Using the interpolated images meant that the pixel location of the target stars was fixed and could be accurately determined from the well-verified astrometry of the reference images (2″ errors relative to Tycho stars at worst, compared to a 16″ FWHM). We do not see any evidence that the interpolation causes problems.

Using the as-reduced images creates the problems seen for the bright Cepheids because of two issues. The first is that an interplay between adding bias corrections and the inheritance from the ASAS pipeline of reading only integer fits files can lead to damaging saturated images because of integer overflows. This manifests as pixels in the star being flagged as bad and given a pixel value of unity. This obviously causes severe problems for the standard aperture photometry pipeline. The MLP pipeline largely manages to correctly interpret the flagged pixels and recover a good estimate of the true flux. While we understand the origin of the problem, a fix is not trivial and has

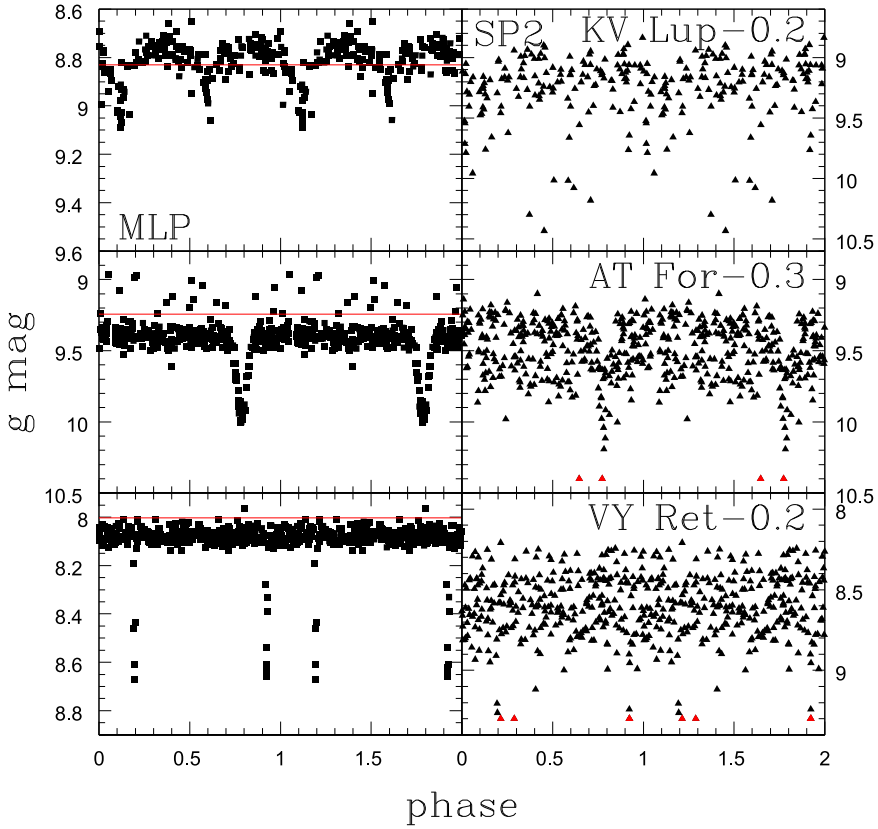

Figure 9. Light curves of eclipsing binaries from the MLP analysis (left) and SSP2 (right). The SP2 light curves are shifted to brighter magnitudes by the amount next to the variable name. The bright magnitude limit is the same for the MLP and SP2 panels, but the magnitude range is generally much larger for the SP2 panels. The red points lying in a line along the bottom are outliers fainter than the minimum magnitudes of the panels. The horizontal red line is the *g* magnitude predicted from the mean Gaia magnitudes. VY Ret has a highly eccentric orbit leading to the asymmetric eclipse phases.

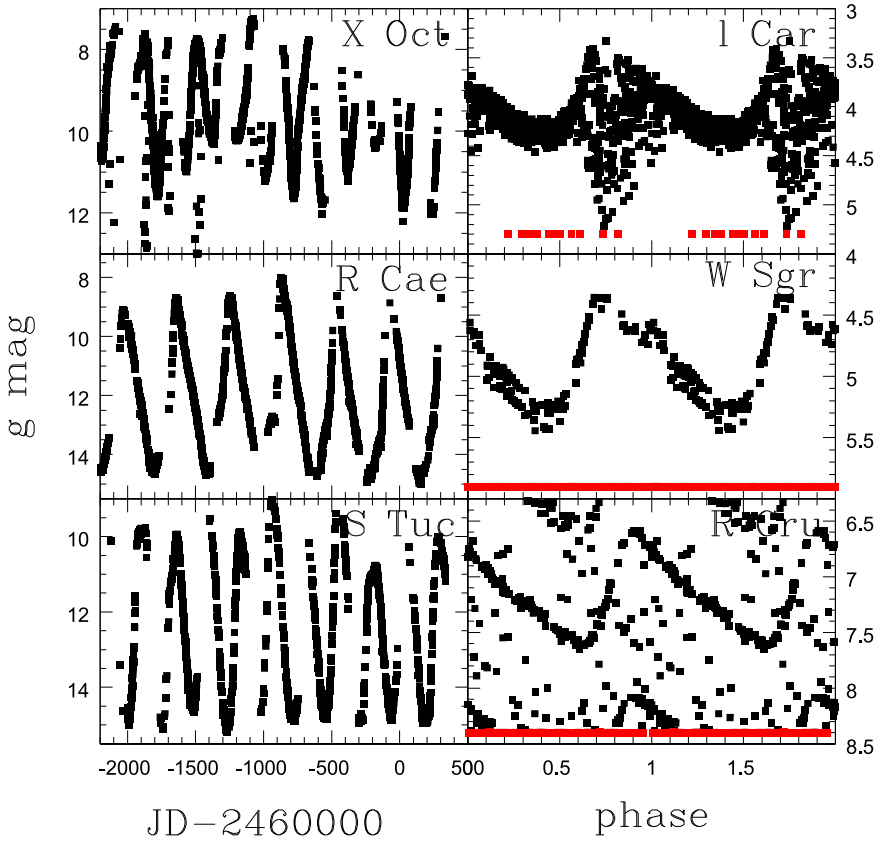

Figure 10. MLP light curves of the Miras and Cepheids from Figures 6 and 7 (black squares) as compared to their MLP light curves using both *V*- and *g*-band data from all the ASAS-SN cameras observing each star. Outliers are marked at the bottom in red.

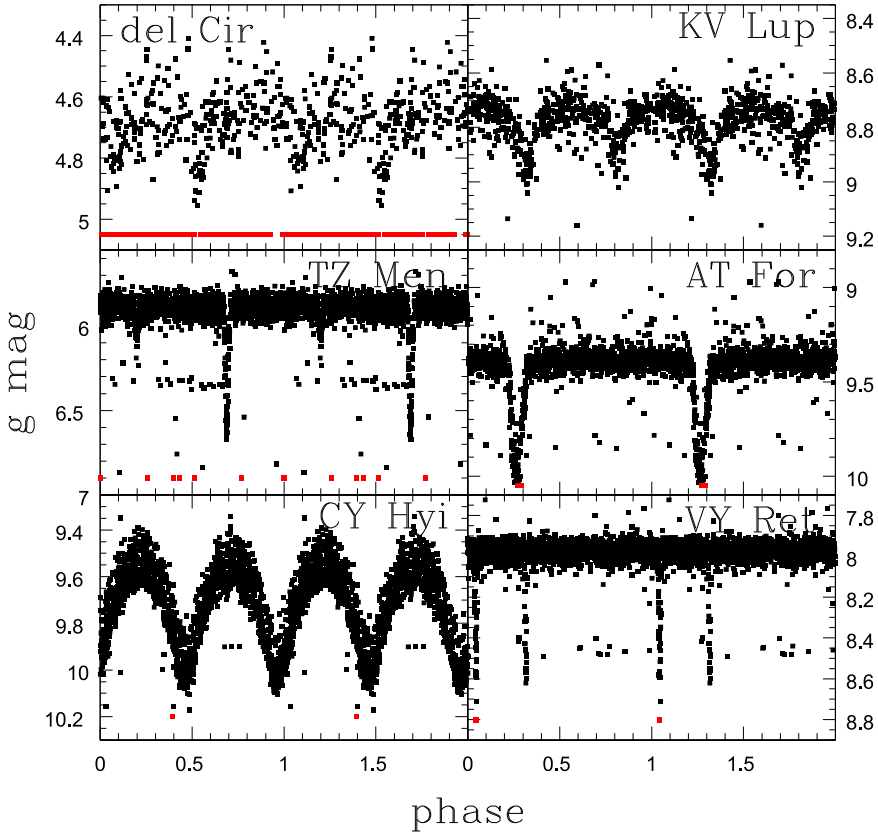

Figure 11. MLP light curves of the eclipsing binaries from Figures 8 and 9 (black squares) as compared to their light curves using both *V*- and *g*-band data from all the ASAS-SN cameras observing each star. Outliers are marked at the bottom in red.

yet to be implemented. We believe the performance of an MLP retrained after the problem is fixed should be improved.

The second problem comes from mistakes made by the saturated star corrections inherited from the ASAS pipeline. As noted earlier, the pipeline tries to collect the flux from the bleed trail and add it as a Gaussian at the location of the saturated star with the FWHM of the data. This generally works very well, but the flux is sometimes assigned to the wrong location and sometimes seems not to be assigned to any location. We see this problem here for the very brightest examples we show (Figures 7, 10, and 11). Determining the origin of these problems in the pipeline is beyond our present scope.

We suspect that our approach would have worked well and avoided this problem using data without these attempts to correct saturated stars. Testing this is, however, an involved process. The original raw images are available, but they would have to be reprocessed without the saturated star corrections (or at least the postage stamp images needed for each star would have to be reprocessed). The pixel positions of stars would also now vary from image to image, so we would need to be fully confident of the astrometry of the individual images. Checking this astrometry has not been a priority because all the current ASAS-SN results depend only on the astrometry of the reference image for a field and not on the astrometry of the individual images.

One likely area where our results could be improved is in the estimation of the predicted counts for the training set. As a reminder, we predicted SDSS *g* magnitudes from Gaia DR3 magnitudes, converted them to counts using the zero-point of the ASAS-SN reference image and the image subtraction estimate of the transparency difference between the images defining the zero-point and the current image, and attempted to correct for the flux from other stars within the large ASAS-SN PSF. The Riello et al. (2021) transformation from Gaia magnitudes to *g* band is not great, with a reported scatter of 0.075 mag. This is, however, not large enough to be a major contributor to the scatter seen for the verification data. Nonetheless, it might be better to have used ATLAS REFCAT (Tonry et al. 2018a) since it was built in part to systematically estimate *g*-band magnitudes.

The crowding corrections were computed based only on the Gaia *G*-band magnitudes, and they should probably have been based on the estimated *g*-band magnitudes. The thought was that these corrections should mostly be small, so the modest fractional errors in them would not be important. Retrospectively, this may be need to be treated more carefully for the nonsaturated stars. There might also be issues from the interplay between the estimated crowding corrections and the size and geometry of the postage stamp images (Figure 1). For the saturated stars, which are the primary target of the project, this is less of an issue simply because the stars are so bright and the standard pipeline performs so poorly. Moreover, the scatter seen for the unsaturated stars in the verification data does not depend on Galactic latitude, which suggests that problems with confusion cannot be a dominant driver of the scatter.

If a primary driver of the scatter was simply the accuracy of the conversion from estimated counts to magnitudes driven by zero-point and transparency errors, then we would expect the fluctuations in the light curves of constant sources lying in the same field to be correlated. If so, this would then lead to a natural approach to improving the image calibrations by using the correlated variability to estimate an image calibration

correction. We inspected this question for the trial light curves of nonvarying sources lying in the same field and found, unfortunately, no obvious correlations.

The most important issues to be addressed are the problems created by the ASAS-SN pipeline, fixing the damage done to the images of saturated stars, and either understanding the failures of the saturated star corrections or switching to using images without the corrections. We need to more extensively test how well the MLP works on multiple cameras to determine if we can simply train a single MLP for all cameras, perhaps with the camera identification as an additional item of metadata.

This method is now available as an option on ASAS-SN Sky Patrol v1.0 (Kochanek et al. 2017) as the "Saturated Stars (Machine Learning)" photometry option.[4] As should be clear from the examples, the results become less predictable for stars approaching naked eye visibility and brighter. The present method supplies no magnitude uncertainties, so these are simply reported as the typical scatter seen in Figure 4. Better error estimates of the relative errors can be derived from the light curves, but this requires some information on the nature of any variability (e.g., periodic or nonperiodic), making it difficult to estimate automatically. We anticipate that the machine learning results will steadily improve, particularly once the reduction pipeline problems for saturated stars are corrected. It is also considerably faster than the most equivalent mode of Sky Patrol v1.0 ("Aperture Photometry"), which takes roughly 5 times longer to produce the light curves shown in Figures 6–9.

Acknowledgments

We thank Dustin Perzanowski of Ohio State's ASCTech group for adding the machine learning option to Sky Patrol v1.0. C.S.K. is supported by NSF grants AST-2307385 and AST-1908570. ASAS-SN is funded in part by the Gordon and Betty Moore Foundation through grants GBMF5490 and GBMF10501 to the Ohio State University, and also funded in part by the Alfred P. Sloan Foundation grant G-2021-14192.

ORCID iDs

Dominik Winecki https://orcid.org/0009-0009-8632-3102
Christopher S. Kochanek https://orcid.org/0000-0001-6017-2961

References

Abdurro'uf, Accetta, K., Aerts, C., et al. 2022, ApJS, 259, 35
Alard, C. 2000, A&AS, 144, 363
Alard, C., & Lupton, R. H. 1998, ApJ, 503, 325
Bellm, E. C., Kulkarni, S. R., Graham, M. J., et al. 2019, PASP, 131, 018002
Eyer, L., Audard, M., Holl, B., et al. 2023, A&A, 674, A13
Gaia Collaboration, Prusti, T., de Bruijne, J. H. J., et al. 2016, A&A, 595, A1
Gaia Collaboration, Vallenari, A., Brown, A. G. A., et al. 2023, A&A, 674, A1
Hart, K., Shappee, B. J., Hey, D., et al. 2023, arXiv:2304.03791
Jayasinghe, T., Stanek, K. Z., Kochanek, C. S., et al. 2019, MNRAS, 486, 1907
Ivezić, Ž., Kahn, S. M., Tyson, J. A., et al. 2019, ApJ, 873, 111
Kim, E. J., & Brunner, R. J. 2017, MNRAS, 464, 4463
Kingma, D. P., & Ba, J. 2014, arXiv:1412.6980
Kochanek, C. S., Shappee, B. J., Stanek, K. Z., et al. 2017, PASP, 129, 104502
Kozłowski, S., Kochanek, C. S., Udalski, A., et al. 2010, ApJ, 708, 927
Page, M. J., Kuin, N. P. M., Breeveld, A. A., et al. 2013, MNRAS, 436, 1684
Pasquet, J., Bertin, E., Treyer, M., Arnouts, S., & Fouchez, D. 2019, A&A, 621, A26
Paszke, A., Gross, S., Massa, F., et al. 2019, in Advances in Neural Information Processing Systems 32, ed. H. Wallach et al. (Red Hook, NY: Curran Associates, Inc.), 8024
Pojmanski, G. 2002, AcA, 52, 397
Qu, H., Sako, M., Möller, A., & Doux, C. 2022, in ICML 2022 Workshop on Machine Learning for Astrophysics, 51
Riello, M., De Angeli, F., Evans, D. W., et al. 2021, A&A, 649, A3
Shappee, B. J., Prieto, J. L., Grupe, D., et al. 2014, ApJ, 788, 48
Su, K. Y. L., Rieke, G. H., Marengo, M., & Schlawin, E. 2022, AJ, 163, 46
Tonry, J. L., Denneau, L., Flewelling, H., et al. 2018a, ApJ, 867, 105
Tonry, J. L., Denneau, L., Heinze, A. N., et al. 2018b, PASP, 130, 064505
Yang, Z., Liu, M., Yuan, H., et al. 2023, AJ, 166, 210
Yuan, H., Liu, M., Yang, Z., et al. 2023, AJ, 166, 244
Zhou, H., Jin, Z.-P., Covino, S., Fan, Y.-Z., & Wei, D.-M. 2023, ApJS, 268, 65

[4] http://asas-sn.osu.edu/